Shi *et al. PhotoniX* (2026) 7:25
https://doi.org/10.1186/s43074-026-00246-2

PhotoniX

RESEARCH **Open Access**

Diagnosis of meibomian gland dysfunction based on spectral convolutional neural network chip

Yue Shi[1,2†], Tianhao Liu[3†], Shan Yang[1,2], Yu Di[1,2], Ying Li[1,2], Weihong Yu[1,2], Yidong Huang[3], Di Chen[1,2*] and Kaiyu Cui[3*]

[†]Yue Shi and Tianhao Liu contributed equally to this work.

*Correspondence:
chendi@pumch.cn;
kaiyucui@tsinghua.edu.cn

[1] Department of Ophthalmology, Peking Union Medical College Hospital, Chinese Academy of Medical Sciences & Peking Union Medical College, Beijing 100730, China
[2] Beijing Key Laboratory of Fundus Diseases Intelligent Diagnosis & Drug/Device Development and Translation, Beijing 100730, China
[3] Department of Electronic Engineering, Tsinghua University, Beijing 100084, China

Abstract

Dry eye disease (DED) is the most common ocular surface disorder with meibomian gland dysfunction (MGD) as a leading cause. However, precise diagnosis of MGD based on the intrinsic composition remains unattainable, leading to delayed diagnosis and suboptimal therapeutic interventions. This study proposes a high-precision hyperspectral pathological diagnosis scheme for MGD based on a real-time spectral convolutional neural network (SCNN) chip. We analyze the spectral characteristics of meibum, hemoglobin, and its derivatives of meibomian gland pathological sections. The neural network trained on the SCNN chip for MGD diagnosis achieved a diagnostic accuracy of 96.22%, outperforming models based on RGB images of 84.00%. To our knowledge, this is the first study to develop a spectral pathological diagnostic model for MGD and to apply optical neural networks for the diagnosis of MGD. This finding offers new possibilities for effective and accurate MGD management and promotes the performance of SCNN chip for medical applications.

Keywords: Spectral convolutional neural network chip, Dry eye, Meibomian gland dysfunction

Introduction

Dry eye disease (DED) has become a critical public health concern, affecting approximately 344 million people worldwide [1]. Severe cases of DED can cause severe impairment to quality of life and a substantial economic burden [2]. It is estimated that around 70% of DED cases are attributed to evaporative dry eye, which is commonly caused by meibomian gland dysfunction (MGD). The meibomian glands, located within the tarsal plates of the upper and lower eyelids, are vertically aligned along the eyelid margins. These glands play a critical role in synthesizing and secreting lipids, which form the outermost layer of the tear film and serve to reduce tear evaporation. MGD is primarily characterized by terminal duct obstruction, acinar atrophy, and qualitative and/or quantitative abnormalities in meibum secretion [3]. Currently, the diagnosis methods of MGD, including symptom assessment and various clinical tests for evaluation of meibomian gland function and morphology, have the problem of subjectivity, lack of specificity, patient discomfort, limited functional correlation, early-stage sensitivity issues, and lack of a gold standard [4]. Accurate diagnosis and quantitative assessment of MGD are fundamental prerequisites for proper medical intervention, significantly impacting patients' visual quality and quality of life. Thus, there is a strong need for more objective, non-invasive, and standardized methods, such as detecting the contents of meibum in clinical practice, to improve the accuracy and efficiency of MGD diagnosis, particularly in the early stages of the disease.

Hyperspectral imaging is an advanced analytical technique for medical applications which can leverage the interaction between light and matter to capture unique spectral "fingerprints" of biological tissues, offering rich biochemical and structural information in a non-contact manner [5]. It has shown promising potential in the field of ophthalmology, particularly for non-invasive oxygen level assessment. By capturing detailed spectral information across different wavelengths, this technology enables precise monitoring of oxygen-related changes in ocular tissues, offering valuable insights into vascular function and eyelid inflammation involved in the pathogenesis and progression of MGD [6, 7]. Considering the limitations of commercial hyperspectral systems such as bulky size and reliance on mechanical scanning, recent efforts have focused on developing snapshot spectral imaging technologies, which significantly expand the applicability of spectral sensing [8–10]. Among them, a metasurface-based snapshot ultraspectral imaging chip has demonstrated real-time, pixel-level spectral acquisition with high accuracy (0.04 nm) and resolution (0.8 nm) [10]. Furthermore, a metasurface-based spectral convolutional neural network (SCNN) chip has shown promise for real-time, in-sensor computing, achieving high accuracy in pathological diagnosis [11]. Spectral analysis holds potential to non-invasively probe biochemical changes in the tear film and meibum composition, offering a pathway toward more accurate, objective, and early diagnosis.

To date, studies focusing on the spectroscopic properties of meibomian gland tissue components remain preliminary. Meibomian gland tissue primarily contains spectrally characteristic components such as meibum, hemoglobin, and its derivatives. In the visible light spectrum, particularly around 550 nm, hemoglobin and its derivatives within biological tissues exhibit distinct absorption characteristics. This results in a pronounced absorption dip in the reflectance spectrum, which serves as a key spectral signature for detecting and quantifying hemoglobin and its derivatives [10, 12]. Previous studies have explored the spectral characteristics of meibum by collecting and purifying it ex vivo, followed by spectral analysis of the isolated samples [13, 14]. However, the optical properties of meibum remain poorly understood. Due to technical limitations in spectral acquisition—where current devices cannot simultaneously achieve high spatial and temporal resolution—quantitative spectroscopic analysis of meibomian gland composition remains challenging.

In this work, we analyze the spectral characteristics of profiles of meibomian gland tissue components in MGD and propose a pathological diagnosis scheme based on a real-time SCNN chip. Firstly, the spectral characteristics of MGD patients and non-MGD patients were obtained from pathological sections, and significant spectral differences were found between the two groups in the 500—900 nm wavelength range. This reflects potential changes in hemoglobin absorption and meibum composition. Then we used the SCNN chip for the spectral acquisition and automatic classification of MGD and non-MGD. The SCNN model achieved over 96% diagnostic accuracy, surpassing models based on both commercial hyperspectral and RGB data. Unlike commercial hyperspectral cameras, which are typically large, slow due to scanning requirements, and costly, the SCNN chip is a miniaturized, snapshot spectral feature extraction and computing system. These findings demonstrate the promise of ultraspectral imaging and SCNN chip for real-time, non-invasive, and high-precision diagnosis of MGD.

Results

Clinical and spectral characteristics

The clinical and spectral characteristics of the participants included are summarized in Table 1. In total, 90 ultraspectral images, 90 hyperspectral images, and 86 RGB images were obtained from the 5 MGD patients, while 95 ultraspectral images, 84 hyperspectral images, and 66 RGB images were collected from the 6 non-MGD controls. Participants with MGD exhibited significantly higher meibomian gland expressibility (MGEX) compared to those without MGD ($P < 0.001$). The tear film break-up time (TBUT) was significantly lower in the MGD group compared to participants without MGD ($P < 0.001$). Significant differences were observed in clinical parameters related to MGD between the participants with MGD and without MGD. Participants with MGD exhibited significantly higher spectral coefficients in the 600–700 nm wavelength range compared to participants without MGD ($P < 0.05$).

Spectral coefficient maps and associated clinical characteristics

Subgroup analyses of spectral coefficients based on various MGD-related clinical parameters are shown in Fig. 1. Participants under 50 years of age exhibited significantly higher spectral coefficients than those aged 50 years or older in the 500–600 nm ($P = 0.03$), 600–700 nm ($P < 0.001$), 700–800 nm ($P < 0.001$), and 800–900 nm ($P < 0.001$) wavelength ranges. The spectral coefficients in females were significantly higher than in males in the 500–600 nm ($P < 0.001$) and 700–800 nm ($P < 0.001$) wavelength ranges. For the wavelength range of 600–700 nm and 800–900 nm, the spectral coefficient showed

Table 1 Comparisons of characteristics in participants with or without MGD

Baseline characteristic	MGD (n = 5)	Non-MGD (n = 6)	*P* value
Age (years)	49.00±20.82	42.83±15.78	0.589
Gender (Female)	4 (80.00)	4 (66.67)	1.000
TBUT (s)	4.20±2.39	9.83±1.33	<**0.001**
CFS (0–12)	0.00 (0.00, 1.00)	0.00 (0.00, 0.00)	0.182
OSDI (0–100)	55.00 (43.00, 57.00)	10.00 (9.25, 11.50)	0.014
MGEX (0–9)	7.60±1.14	2.50±0.84	<**0.001**
Meibum quality (0–3)	2.00 (2.00, 3.00)	0.00 (0.00, 0.75)	0.100
Spectra Coefficient			
500–600 nm	0.24±0.10	0.22±0.09	0.739
600–700 nm	0.21±0.04	0.13±0.06	**0.036**
700–800 nm	0.21±0.15	0.25±0.09	0.651
800–900 nm	0.10±0.02	0.05±0.04	0.079

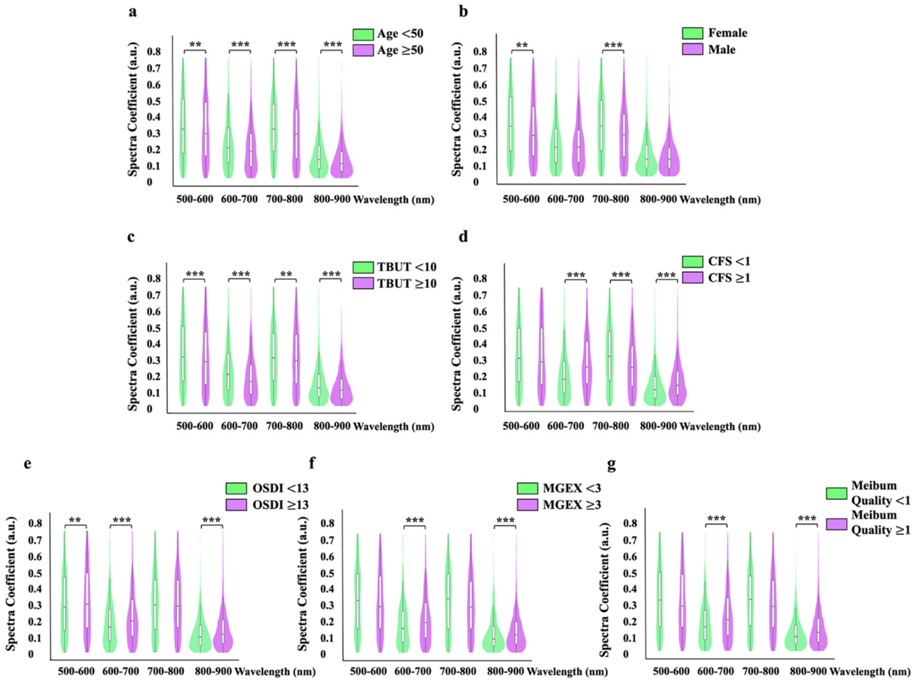

Fig. 1 Subgroup analysis of the Spectra Coefficient. **a** Spectral characteristics of age subgroups. **b** Spectral characteristics of gender subgroups. **c** Spectral characteristics of tear film break-up time (TBUT) subgroups. **d** Spectral characteristics of corneal fluorescein staining (CFS) subgroups. **e** Spectral characteristics of ocular surface disease index (OSDI) subgroups. **f** Spectral characteristics of meibomian gland expressibility (MGEX) subgroups. **g** Spectral characteristics of meibum quality subgroups

statistically significant differences between TBUT score ≥ 10 group and < 10 group ($P< 0.001$; for results using 5-s and 8-s cut-offs, see Supplementary Material 2), between corneal fluorescein staining (CFS) score ≥ 1 group and < 1 group ($P< 0.001$), between ocular surface disease index (OSDI) score ≥ 13 group and < 13 group ($P< 0.001$), between MGEX score ≥ 3 and < 3 group ($P< 0.001$), between meibum quality score ≥ 1 group and < 1 group ($P< 0.001$).

Representative light microscopy images of the Hematoxylin and eosin (H&E)-stained meibomian gland sections from MGD and non-MGD participants are shown in Fig. 2, along with the corresponding feature maps generated by the optical convolutional neural network. The measured spectral coefficient maps of the meibomian gland (MG) region and non-MG region are shown in Fig. 3. The graphs in Fig. 3 indicate the median values of the spectral coefficients for each group. The spectral coefficients of the MG region in the MGD group were significantly higher than those in the non-MGD group in the 500–600 nm ($P<005$), 600–700 nm ($P<0.05$, and 800–900 nm $P<0.001$) wavelength ranges. Similarly, the spectral coefficients of the non-MG region in the MGD group were significantly higher than those in the non-MGD group in the 500–600 nm ($P<005$), 600–700 nm ($P<0.05$, and 800–900 nm $P<0.001$) wavelength ranges. Additionally, MGD patients exhibited significantly lower spectral coefficients in the 800–900 nm ($P<0.01$) wavelength range in the MG region compared to the non-MG region. In the non-MGD group, the spectral coefficients in the MG region were also significantly lower than those in the non-MG region in the 800–900 nm ($P<0.05$) wavelength range (Fig. 3).

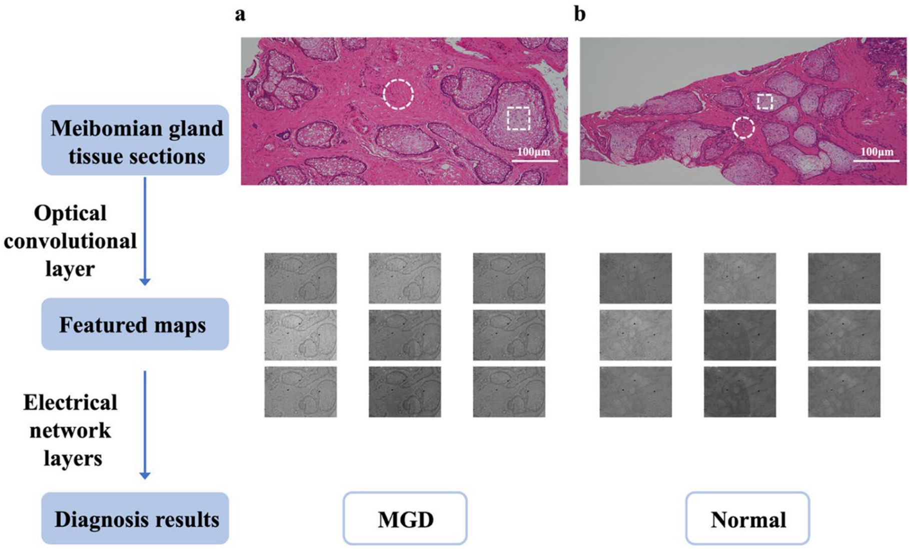

Fig. 2 The hematoxylin and eosin-stained tissue sections and the corresponding feature maps of human meibomian gland in participants with and without meibomian gland dysfunction (MGD). **a** In participants with MGD, the sections exhibit relatively fewer acini (white square) and an increased proportion of connective tissue (white circle). **b** In participants without MGD, the histopathologic sections show a higher density of acini (white square) with well-preserved structures and a reduced presence of connective tissue (white circle)

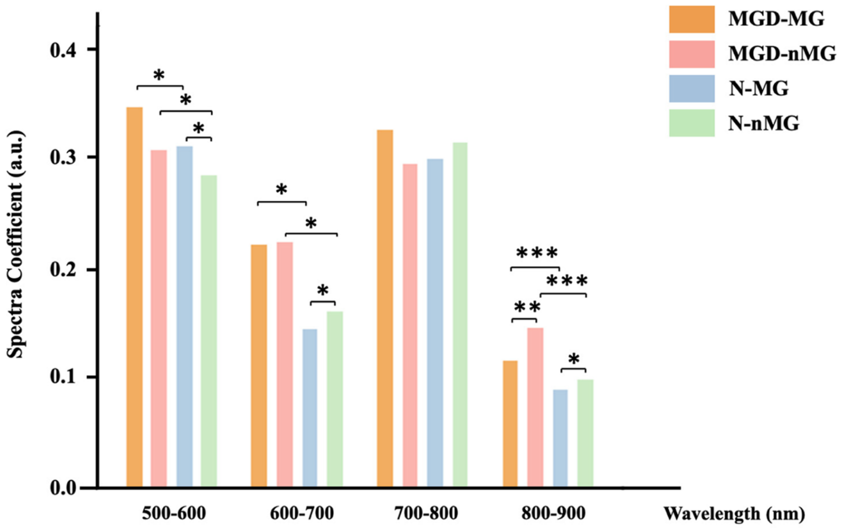

Groups	500-600	600-700	700-800	800-900
MGD-MG	0.346 (0.170, 0.583)	0.220 (0.124, 0.388)	0.325 (0.166, 0.500)	0.114 (0.057, 0.216)
MGD-nMG	0.307 (0.168, 0.522)	0.223 (0.125, 0.390)	0.294 (0.168, 0.480)	0.144 (0.075, 0.231)
N-MG	0.310 (0.148, 0.508)	0.143 (0.071,0.237)	0.298 (0.150, 0.237)	0.088 (0.040, 0.149)
N-nMG	0.284 (0.150, 0.457)	0.159 (0.071,0.287)	0.314 (0.142, 0.488)	0.097 (0.045, 0.179)

Fig. 3 Comparison of the spectra coefficient of the meibomian gland dysfunction (MGD) groups and the control. MGD-MG is meibomian gland (MG) region in participants with MGD; MGD-nMG is non- MG region in participants with MGD; N-MG is MG region of participants without MGD; N-nMG is non-MG region of participants without MGD. (*: $p < 0.05$, **: $p < 0.01$ **: $p < 0.001$)

The SCNN classification model

We conducted classification experiments on the collected samples using SCNN to distinguish between MGD and non-MGD cases. For comparison, hyperspectral images captured by a commercial spectrometer and RGB images acquired by a standard RGB camera were also used as input to shallow neural networks similar to the ENLs, and the corresponding classification results were obtained. The performance of the three solutions is presented in Fig. 4. The SCNN model achieved an average accuracy of 96.22%, with average precision of 96.34%, average recall of 96.29% and average F1-score of 96.22%. The CNN model using commercial spectral images as input achieved an average accuracy of 95.88%, with average precision of 89.74%, average recall of 91.88% and average F1-score of 90.78%. The average accuracy of the CNN model using RGB images (84.00%) as input was lower than that achieved with spectral images as input. The receiver operating characteristic (ROC) curves of the Convolutional Neural Networks model using SCNN images, commercial spectral images, and RGB images in Monte Carlo cross-validation are described in Supplementary Material 3.

Discussion

To our knowledge, this study pioneers the first global investigation of meibomian gland spectrum. Our analysis revealed statistically significant differences in spectral coefficients between patients with MGD and without MGD across three clinically relevant wavelength bands: 500–600, 600–700, and 800–900 nm. These spectral variations may

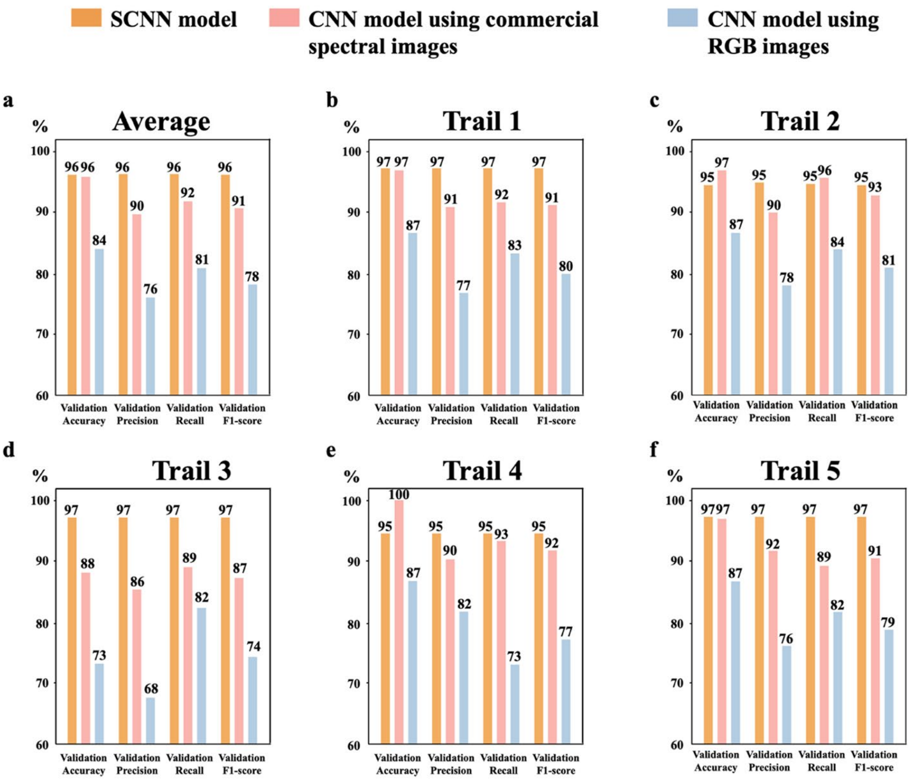

Fig. 4 Performance of the spectral convolutional neural network (SCNN) model under Monte Carlo cross validation. CNN is convolutional neural network

be associated with changes in hemoglobin-related compounds and meibum components, although further validation is needed to confirm specific pathophysiological mechanisms. Furthermore, this study established, to our knowledge, the first spectral database of pathological sections of meibomian glands from MGD patients, which represents a major advancement in ocular surface diagnostics. Leveraging this database, our spectral neural network classification model achieved remarkable diagnostic accuracy of 95.88%, representing an absolute improvement of 11.88% over conventional RGB image analysis. These results underscore the superior diagnostic potential of spectral fingerprinting over traditional imaging methods for the pathological diagnosis of ocular surface disease. Furthermore, this study demonstrates a metasurface-based SCNN system that achieves a diagnostic accuracy of 96.22%, comparable to that of commercial hyperspectral imaging systems. In contrast to conventional devices, which require tens of seconds for spectral acquisition, the SCNN reduces acquisition time to mere tens of milliseconds. Its compact architecture offers promising potential for integration into portable platforms, enabling real-time, in vivo diagnosis of MGD and thereby improving the speed and precision of clinical workflows.

The significant spectral differences between MGD and non-MGD groups across multiple wavelength ranges suggest distinct compositional variations in meibomian gland tissues. MGD, a chronic inflammatory disease, increases oxygen demand within meibomian gland tissue, leading to changes in the concentration and properties of hemoglobin and its derivatives in local blood flow [15, 16]. Hemoglobin (Hb) and its derivatives, including oxyhemoglobin (HbO_2) and carboxyhemoglobin (HbCO), exhibit significant absorption characteristics in the range of 500 nm to 600 nm [17, 18]. Previous studies utilized a Spatial Frequency Domain Imaging (SFDI) system to detect the Hb concentration and changes in the optical properties at 630 nm for the MG and non-MG regions in the MGD rat model [15]. These unique spectral properties make hemoglobin and its derivatives highly valuable in spectroscopic detection. Xiong et al. [10] demonstrated that spectral variations obtained from different regions of the rat brain can be utilized to assess changes in the concentrations of hemoglobin and its derivatives in both vascular and non-vascular areas. Furthermore, utilizing the neurovascular coupling mechanism, this approach enables the inference of neuronal activity within the brain. In our study, the spectral coefficients in the 500–600 nm and 600–700 nm range were significantly increased in both the MG and non-MG regions of pathological sections from MGD patients compared to healthy controls. Moreover, the spectral coefficients in this wavelength range exhibited significant differences across both age groups and MGD-related clinical assessment categories, especially in the range of 600–700 nm. Furthermore, higher spectral coefficients were observed both in younger patients and in those with more severe dry eye-related symptoms. Since the optical setup in this study measured transmission spectra, the increased spectral coefficients suggest a relatively reduction in absorption within this wavelength range in MGD patients. Consistent with this, one possible explanation is that these changes reflect alterations in local hemoglobin properties or concentration. Liu et al. [19] have previously reported that a relatively hypoxic environment is beneficial for the normal functioning of meibomian glands. While our findings are consistent with the possibility of altered oxygen-related processes, further studies are needed to determine whether the observed spectral changes directly reflect compensatory mechanisms or other adaptive responses. Collectively, these results highlight the potential of hyperspectral analysis as a powerful tool to explore the pathophysiological changes in MGD.

Meibum, a complex mixture of various lipids secreted by the meibomian glands, is a critical component of the outermost layer of the tear film [13]. It plays essential physiological roles, such as reducing tear evaporation and protecting the cornea and conjunctiva. Meibum is primarily composed of polar and non-polar lipids. Among the polar lipids, phospholipids account for approximately 70%, whereas the non-polar lipids are predominantly composed of wax esters and cholesteryl esters [20]. It is challenging to measure lipid concentration using conventional microscope light sources, which mainly cover the visible light spectrum. In our study, significant spectral differences between MGD patients and healthy controls were observed in the near-infrared (NIR) range of 800–900 nm within the meibomian gland region. Additionally, spectral variations were detected between the MG region and non-MG regions in MGD patients. Furthermore, spectral absorption coefficients within this wavelength range were found to be associated with age, tear film stability, and meibomian gland functional parameters. Hwang et al. reported that light transmission through the acini of human MG is significantly reduced compared to other eyelid tissues, such as muscle and dermis. This reduction in transmission is primarily attributed to light scattering caused by the lipid-rich components within the meibomian glands [21]. In addition, several studies have conducted ex vivo spectral measurements of human meibum to investigate alterations in its chemical structure and intermolecular interactions [14, 22]. Nuclear magnetic resonance (NMR) spectroscopy combined with principal component analysis differentiated MGD patients' meibum in vitro from normal meibum with 86% accuracy, detecting significantly reduced levels of CH_3 groups, lipid oxidation products, and terpenoid-associated compounds in MGD samples [23]. Raman spectroscopy has identified near-equivalent lipid saturation meibum from MGD patients and normal participants but detected progressive carotenoid depletion with age in MGD. However, both Raman and NMR spectroscopy are limited to single-point spectral acquisition, inherently lacking spatial imaging capability and precluding real-time spectral mapping of targeted areas. The silicon-based metasurface SCNN chip enables snapshot acquisition of microscopic spectral feature maps from meibomian gland pathological tissue sections. This approach may facilitate future investigations into meibum compositional dynamics during MGD progression, potentially contributing to the development of non-invasive diagnostic and monitoring tools.

In current deep learning research related to meibomian glands, the primary approach involves using standard RGB images to train neural network models for identifying the degree of glandular atrophy in different patients [24, 25]. This provides clinicians with a quantitative assessment of morphological changes in the meibomian glands. However, our study utilizes spectral data from meibomian glands to develop a neural network model. Spectral data provide additional information beyond conventional RGB imaging, which may contribute to improved classification performance. The key advantage of metasurface-based SCNN cameras lies in their ability to simultaneously capture spatial and spectral information, thereby enhancing data dimensionality and enabling superior CNN model prediction performance. Our results demonstrate that SCNN achieves performance comparable to the model trained on commercial spectral images, while significantly outperforming the RGB-based model across multiple metrics, including accuracy, precision, recall, and AUC. The combination of spatial and spectral information may enable a more comprehensive evaluation of meibomian gland tissue properties, potentially benefiting early detection and monitoring of MGD. These results demonstrate that the spectrum obtained from pathological sections of the meibomian gland provides reliable features for the accurate diagnosis of MGD. Spectral analysis thus holds promise for simplifying the diagnostic workflow and enhancing clinical diagnostic efficiency. In contrast to commercial hyperspectral cameras, which typically require tens of seconds to capture a single hyperspectral image, the SCNN system can generate a spectral feature map within tens of milliseconds—comparable to the exposure time of conventional RGB cameras. This substantial improvement addresses the critical limitation of commercial hyperspectral cameras: their prolonged acquisition time renders them unsuitable for real-time in vivo clinical applications, as they cannot: (1) compensate for ocular micro-movements during measurement, (2) capture dynamic biological processes, or (3) meet the time constraints of routine clinical diagnostics. Furthermore, benefiting from the in-sensor computing architecture of the OCL, the SCNN enables ultrafast and low-power execution of MGD pathological diagnosis tasks. It achieves diagnostic accuracy comparable to that of commercial hyperspectral cameras, while offering the potential for integration into miniaturized systems for in vivo MGD diagnosis. This significantly enhances both the efficiency and accuracy of clinical diagnostics. Furthermore, the success of our spectral-based CNN model highlights the potential of combining advanced imaging techniques with machine learning for improving diagnostic accuracy in ophthalmology.

This study has several limitations that should be acknowledged. First, this retrospective analysis used meibomian gland tissues collected in 2020. Although we demonstrate that stable spectral data can be reliably obtained from archival specimens, the ex vivo processing—including sectioning and preparation—may alter key components such as hemoglobin and meibum, potentially affecting spectral measurements. Additionally, the spectral signatures represent a "snapshot" at the time of fixation rather than dynamic physiological states. To address these limitations, future studies should aim to develop real-time, in vivo spectral imaging techniques. Given the compact architecture and rapid acquisition speed of the SCNN chip demonstrated in this study, one promising direction is its miniaturization and integration into clinical slit-lamp systems, which could enable non-invasive, in vivo spectral assessment of meibomian glands during routine eye examinations. Second, the sample size in this work ($N = 11$) represents a limitation, reducing statistical power and prompting necessary caution regarding the generalizability of our findings. To mitigate this, we implemented a patch-based augmentation strategy, dividing spectral images into 40×40 pixel patches for training. This approach effectively increased the diversity of training samples while preserving local tissue morphology. Importantly, the final model was evaluated on the original, uncropped images and achieved excellent classification accuracy, underscoring the robustness of the learned representations. These findings lay a critical foundation for future efforts, which will prioritize the assembly of larger, multi-institutional spectral cohorts and the development of more sophisticated AI architectures to advance the field toward clinically viable diagnostic tools. Third, to achieve a more detailed investigation of the spectral characteristics of different lipid components in meibum, additional studies using a 900–1700 nm NIR spectral acquisition system are required. This extended spectral range could provide deeper insights into the molecular composition and interactions of meibum, thereby enhancing our understanding of its role in MGD and improving diagnostic precision. Fourth, although the SCNN-based system and the commercial push-broom hyperspectral system differ in spectral channels, optical configurations, and noise characteristics, the commercial system represents a widely used benchmark for spectral image analysis. The comparison was not intended as a strictly parameter-matched evaluation, but rather as a practical reference against an established spectral imaging modality. Notably, despite its compact snapshot architecture and substantially simplified hardware configuration, the SCNN-based system achieved comparable classification performance, demonstrating its effective spectral feature extraction and analysis capability. Fifth, all tissue samples were obtained from eyelid nevus excision cases, which may not fully represent typical MGD pathology in the general population. This selection bias should be considered when interpreting the findings, and caution is needed in generalizing the results.

Conclusion

In conclusion, this study represents, to our knowledge, the first investigation into the spectral characteristics of pathological sections of meibomian glands in patients with MGD using a hyperspectral camera and SCNN chip. We identified disease-specific spectral signatures in MGD patients within key wavelength ranges, which may be associated with changes in hemoglobin and meibum composition. Furthermore, this study is the first to integrate spectral data from meibomian gland pathological sections with AI, developing a spectral-based diagnostic framework for MGD using ex vivo samples, and implementing in-sensor classification using the SCNN system. This work not only establishes a proof-of-concept for spectral-based MGD detection on pathological sections and demonstrates the potential of SCNN technology for further exploration in ocular surface disease research.

Methods

Patient enrollment

This retrospective study included patients who underwent eyelid pigment nevus resection surgery at the Department of Ophthalmology, Peking Union Medical College Hospital, during June 2020 and December 2020. In accordance with the International Workshop on MGD guidelines [26], the diagnosis of MGD is established if the patient met at least two of the following criteria: (1) eyelid margin abnormalities (eyelid margin morphology and MG orifices), (2) abnormal meibum secretion (e.g. expressibility and meibum quality), (3) dry eye-related ocular symptoms, (4) structural abnormalities of the MG, and (5) abnormal tear film lipid layer thickness. Patients with diabetes and autoimmune diseases were excluded. The following ocular surface parameters were recorded: TBUT, CFS, MG expressibility, and meibum quality scores. All participants were also requested to complete the OSDI scale. This study was approved by the Institutional Review Board of Peking Union Medical College Hospital, Beijing, China (Approval No. ZS-3516). Written informed consent was obtained from each participant specifically for research participation, including the use of their clinical data and excised tissue specimens for this study.

During the surgical excision of eyelid margin nevi in each patient, excess eyelid tissue was carefully collected. Using fine ophthalmic forceps, MG tissue was meticulously dissected from the excised tissue. Excess connective and adipose tissue surrounding the MG was removed using ophthalmic scissors. The anatomical origin of each specimen, including the eye (left or right) and eyelid (upper or lower), was recorded. Timely fix, dehydrate, and wax-embed the tissue, use a paraffin slicer for continuous sectioning, select ideal tissue slices after baking, and store them at room temperature for future use. The dissected meibomian gland tissue was promptly fixed in 10% neutral buffered formalin to preserve cellular morphology. Following fixation, the tissue underwent a standard dehydration process using a graded series of ethanol solutions, followed by clearing in xylene. The dehydrated tissue was then embedded in paraffin wax. Serial sections of the paraffin-embedded tissue were cut using a paraffin slicer. Ideal tissue slices were selected after baking and were stored at room temperature for spectral imaging. The standardized and timely processing of all samples immediately upon collection in 2020 ensures the preservation of tissue integrity and minimizes any potential variation in spectral properties due to differences in sample handling.

The SCNN chip

The SCNN architecture comprises an optical convolutional layer (OCL) and a series of electronic neural layers (ENLs). The OCL is physically realized by coupling a metasurface array chip with a complementary metal oxide semiconductor (CMOS) image sensor (CIS), while the ENLs are implemented in software on a computer [9].

The OCL consists of an array of $H \times W = 175 \times 123$ identical optical convolutional units (OCUs), with each OCU incorporating $K = 3 \times 3$ convolution kernels (Fig. 5a). As a result, the OCL produces a spectral feature map of dimensions $H \times W \times K = 175 \times 123 \times 9$ (Fig. 5b). Each convolution kernel comprises a periodically arranged metasurface structure and underlying CIS pixels. Taking a single OCU as an example, each metasurface performs a Hadamard product between its transmission spectrum $w_i(\lambda)$ and the incident spectrum $x(\lambda)$, while the CIS pixels integrate the transmitted spectral intensities across wavelengths. This process effectively computes the inner product between the incident light spectrum and the transmission spectrum of the metasurface, yielding the output $v = \int w_i(\lambda) \cdot x(\lambda) d\lambda$ (Fig. 5c). Here, i denotes the index of the convolution kernel within the OCU, ranging from 1 to 9. It can be seen that in the OCL, the input is the hyperspectral data cube of the imaged object with dimensions $H \times W \times C$, where C is the number of spectral sampling points. The network weights correspond to the transmission spectra of the metasurfaces in each convolution kernel, and the output is a spectral feature map of size $H \times W \times K$. The metasurface structures used in the convolution kernels within each OCU are consistent with those adopted in our previous SCNN design [9], and are meticulously engineered to produce distinct transmission spectra, thereby enabling effective and discriminative spectral feature extraction (Figs. 5d). Figure 5e presents the t-distributed Stochastic Neighbor Embedding (t-SNE) embedding of the measured transmission spectra from the nine-channel metasurface. Despite some fluctuations in the feature space caused

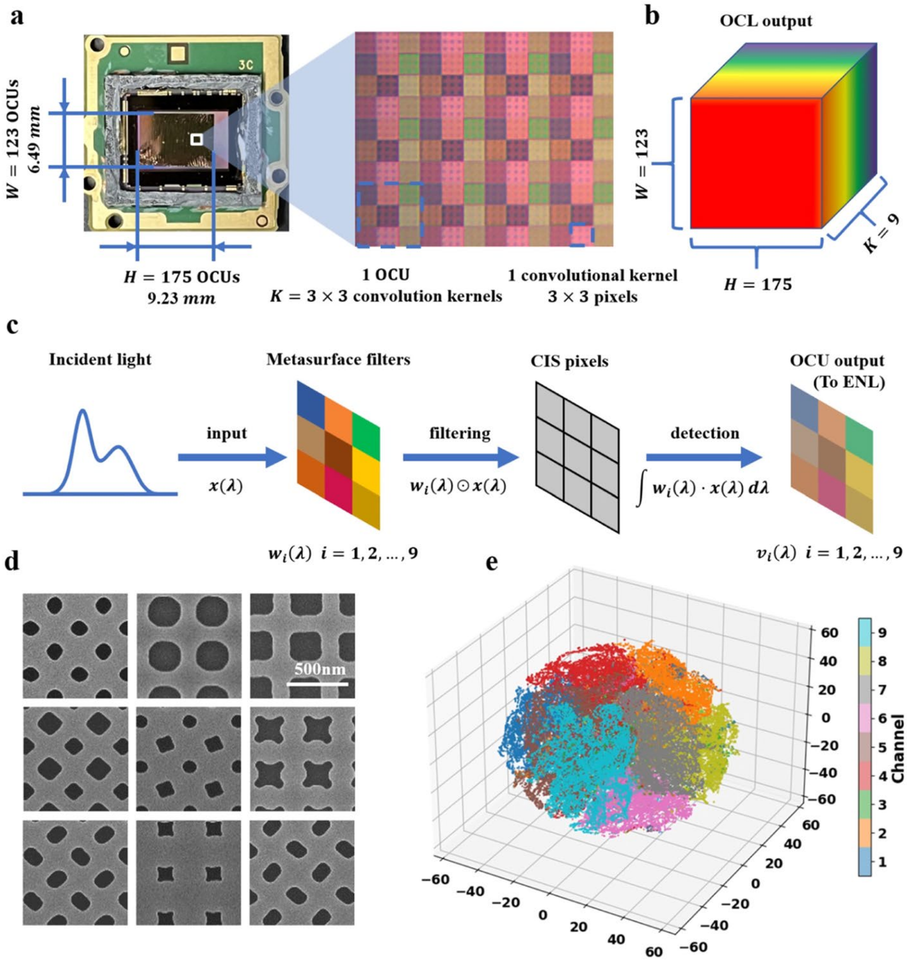

Fig. 5 Principle of the spectral convolutional neural network (SCNN) chip. **a** Photograph and optical microscope image of the SCNN chip. The chip consists of $H \times W = 175 \times 123$ optical convolutional units (OCUs), each OCU comprising $K = 3 \times 3$ convolution kernels. Each kernel consists of a metasurface with a specific nanostructure and a corresponding 3 × 3 pixel region of the complementary metal oxide semiconductor (CMOS) image sensor (CIS). **b** Output spectral feature map from the optical convolutional layer (OCL). The 2D image captured by the CIS is reshaped into a data cube with dimensions $\mathrm{H} \times \mathrm{W} \times \mathrm{K} = 175 \times 123 \times 9$. **c** In-sensor computing principle of a single OCU in the OCL layer. The input signal, represented by the incident spectrum $x(\lambda)$, undergoes a Hadamard product with the transmission spectra $w_i(\lambda)$ of the 9 metasurfaces. The resulting intensities are integrated by the CIS pixels beneath each metasurface, producing $v_i(\lambda)$, which is then sent to the electronic neural layer (ENL) for further processing. **d** Scanning electron microscope (SEM) images of the nine designed metasurfaces. The metasurfaces are carefully engineered to produce distinct and diverse spectral modulation profiles in the visible range. **e** T-distributed stochastic neighbor embedding (t-SNE) embedding visualization of the measured transmission spectra from the nine-channel metasurface

by fabrication-induced variations, the extracted features still exhibit clear distinctions among the nine channels, demonstrating the strong spectral feature extraction capability of the OCUs.

After in-sensor computation by the OCL, the extracted feature maps $H \times W \times K$ are forwarded to the pre-trained ENLs. For the classification of MGD and non-MGD, the ENLs are implemented as a convolutional neural network (CNN), which consists of four convolutional blocks followed by a fully connected classification head. It is worth noting that while the weights of the OCL are fixed after metasurface fabrication, the weights of the ENLs remain fully trainable, offering flexibility to adapt the SCNN architecture to various application scenarios.

Acquisition of spectral images

We designed the hyperspectral imaging system (Fig. 6) to capture spectral data from meibomian gland pathological sections. Figure 6a shows the physical setup of the imaging system, Fig. 6b illustrates the optical path diagram, Fig. 6c presents a schematic of the reconstructed spectral curve, and Fig. 6d depicts the architecture of the SCNN network. Commercial spectral images were acquired using the GaiaField Pro V10 hyperspectral imaging system (Shuangli Hepu, Sichuan, China), a commercial-grade spectral camera designed for high-resolution imaging. Spectral feature maps were acquired using the metasurface-based camera. The metasurface structures were fabricated on a silicon-on-sapphire substrate with a 220-nm-thick top silicon layer. Electron-beam lithography was employed to define the metasurface patterns, followed by inductively coupled plasma etching to transfer the design into the silicon layer. Subsequently, the buried silicon dioxide layer was selectively removed using buffered hydrofluoric acid wet etching, releasing the patterned silicon metasurface. To integrate the metasurface with the CMOS image sensor, the fabricated metasurface was transferred and bonded onto the CIS surface using a polydimethylsiloxane adhesion layer. A commercially available Basler acA1920-40um camera was utilized as the CIS platform. The entire fabrication process is compatible with standard CMOS technology, ensuring scalability and cost-effectiveness for mass production. The system was employed to capture hyperspectral images and spectral feature maps of pathological sections of meibomian gland under a Nikon optical microscope (Fig. 6a). Conventional RGB images of the pathological sections were also acquired under the microscope for comparative analysis.

This study comprised 11 subjects, including 5 diagnosed with MGD and 6 age-matched healthy controls. For each participant, 2–4 pathological sections of

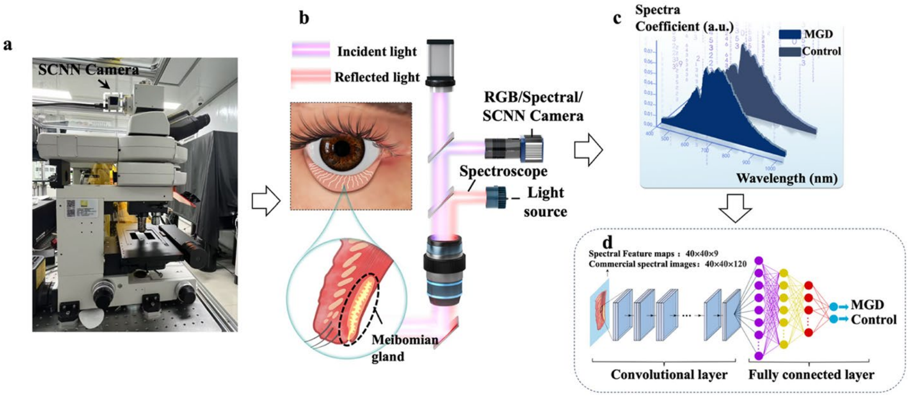

Fig. 6 A schematic overview of the research process. **a** Spectral feature map of meibomian gland tissue sections acquired using a metasurface-based spectral convolutional neural network (SCNN) camera (arrowhead) integrated with an optical microscope. Control is participants without MGD. **b** Experiment setup for pathological section of meibomian gland spectral imaging. **c** Diagram examples of measured spectral intensity data of pathological sections from participants with or without meibomian gland dysfunction (MGD). **d** Schematic representation of the convolutional neural network architecture for classification

meibomian gland tissue were prepared. Depending on the size of the pathological tissue, 5–10 spectral images were captured per section. The spatial resolution of the commercial spectral images acquired was 480 × 550 pixels. The spectral data for the images spanned a wavelength range from 385.7 to 1005.6 nm, comprising 719 wavelength points. The resolution of the SCNN images acquired was 1575 × 1107 pixels, and after screening and reshaping, spectral feature maps of size 175 × 123 × 9 were obtained. Details of the screening algorithm are provided in Supplementary Material 4.

Analysis of spectral data

A series of preprocessing steps was performed on the raw spectral data to facilitate subsequent pathological classification. Due to the low light intensity in the spectral range below 450 nm from the microscope light source, only commercial spectral data between 450 and 1000 nm were considered as valid feature wavelengths. This corresponds to 636 wavelength points from the original 719 wavelength points in the commercial spectral data vector. Considering the spatial inhomogeneity of the microscope light source intensity distribution, the raw commercial spectral data for each pixel were normalized to account for this variation. The absolute light intensity values were converted into relative intensity values, scaled to a range between 0 and 1. The specific normalization process is as follows:

Let the *w*-dimensional spectral data for the *i-th* pixel be represented as:

$$X_i = [x_{i1}, x_{i2}, \cdots, x_{iw}];$$
$$t_i = \sqrt{X_{i1}^2 + X_{i2}^2 + \cdots + X_{iw}^2}$$

The normalized spectral data for the i-th pixel is given by:

$$X_{i\_Norm} = \frac{1}{t}[x_{i1}, x_{i2}, \cdots, x_{iw}]$$

The proposed OCL architecture processes three-dimensional raw hyperspectral data cubes as its primary input. The OCL performs simultaneous optical sensing and convolutional computation through an array of nine specialized convolutional kernels, each with a compact 3 × 3 configuration and an optimized stride length of nine. Following the initial optical processing stage, the generated feature maps undergo subsequent refinement through dedicated electrical processing layers implemented on a central processing unit. This hybrid optical-electronic architecture ultimately produces high-resolution pixel-level detection outputs with dimensions of 175 × 123 × 9, enabling precise spatial characterization of spectroscopic features. For each participant, 100 random pixel points were selected from both the meibomian gland region and the non-meibomian gland region in the pathological sections. Prior to spectral analysis, baseline correction was performed by subtracting the mean spectral value across the entire measured wavelength range from each data point to minimize background noise and ensure comparability across measurements. The area under the spectral curve (AUC) was then calculated using the trapezoidal integration method for each pixel across the following wavelength ranges: 500–600, 600–700, 700–800, and 800–900 nm. This AUC value was defined as the spectral coefficient for that pixel within the corresponding wavelength range.

Statistical analysis

Normality of the data distribution was assessed using the Shapiro–Wilk test. Variables that followed a normal distribution were expressed as mean ± standard deviation, while variables that did not meet the assumption of normality were presented as median and interquartile range. For demographic and clinical data comparisons, parametric variables were analyzed using the two-tailed Student's t-test, while non-parametric variables were compared using the two-tailed Wilcoxon rank sum test. Categorical variables were analyzed using the chi-square test or Fisher's exact test. For spectral coefficient comparisons between groups, the two-tailed Wilcoxon rank sum test was applied, as the spectral data did not satisfy the normality assumption. To control for multiple comparisons, P-values were adjusted using the false discovery rate (FDR) method. Adjusted P-values < 0.05 were considered statistically significant. For heatmap visualization, statistical significance was assessed at each pixel point using the same non-parametric tests, and P-values were adjusted for multiple comparisons using the FDR method to control for Type I errors.

For subgroup analyses, the following cut-off values were selected based on established clinical guidelines and literature: (1) TBUT was analyzed using multiple clinically relevant thresholds: 10 s (diagnostic cut-off for dry eye) [27], 8 s (upper limit of borderline range) [28], and 5 s (indicating severely reduced tear film stability) [29]. (2) Age categorization at 50 years was based on previous studies demonstrating its relevance as a threshold for meibomian gland changes, with morphological and functional alterations becoming more pronounced after the fifth decade [30, 31]; (3) CFS divided at 1 is consistent with clinical grading scales where a score ≥ 1 indicates clinically significant corneal staining [32]; (4) OSDI categorized at 13 was based on the diagnostic threshold for symptomatic dry eye [33]; (5) MGEX dichotomized at 3 reflects severely reduced gland function [34]; and (6) meibum quality divided at 1 indicates abnormal secretion [4]. A p-value of less than 0.05 was considered statistically significant. All statistical analyses were performed using R software (version 4.2.1).

Convolutional neural network training and evaluation

The 636-dimensional spectral vectors after data preprocessing of commercial spectral images still exhibit significant correlation. Directly feeding these vectors into the neural network for training would result in input data redundancy, potentially affecting the efficiency of feature extraction by the neural network. Therefore, Principal Component Analysis (PCA) was applied to reduce the dimensionality of the commercial spectral data. This approach effectively retains the essential feature information while reducing feature correlation, eliminating redundant information, and improving both memory utilization and feature extraction efficiency. Detailed descriptions of the PCA methodology are provided in Supplementary Material 1.

To minimize the presence of blank areas in the pathological images input into the neural network, a 300 × 300 effective region was cropped from the commercial spectral images with a resolution of 500 × 480 pixels. For each cropped commercial spectral image, a sliding window with a step size of 40 pixels was used to extract 40 × 40 pixels subregions, resulting in 196 sub-images for each image. For each spectral feature map, a sliding window with a step size of 10 pixels was used to extract 40 × 40 pixels subregions, resulting in 126 sub-images for each image.

The sub-images were input into the CNN. The reduced spectral image data still preserved the microscopic morphological characteristics of the corresponding pathological sections. The dimension of each commercial spectral image is 40 (pixels) × 40 (pixels) × 196 (wavelength channels). The dimension of each spectral feature map is 40 (pixels) × 40 (pixels) × 9 (channels). In the model training process, dataset splitting was performed at the whole-slide image level. For commercial spectral images, 80% of the whole-slide images (141 images) were randomly selected as the training set, while the remaining 20% (35 images) were used as the validation set. Each training iteration utilized 196 sub-images extracted from each training image, resulting in a total of 27,636 training samples. The validation set yielded 6,860 validation samples (35 images ×196 sub-images). For spectral feature maps, 80% of the whole-slide images (148 images) were assigned to the training set, and the remaining 20% (37 images) to the validation set. Each training iteration utilized 126 sub-images extracted from each training image, resulting in a total of 18,648 training samples. The validation set yielded 4,662 validation samples (37 images ×126 sub-images). To evaluate classification accuracy at the whole-slide image level, a patch-wise voting strategy was employed. To further assess model robustness under the limited cohort size, Monte Carlo cross-validation was performed at the whole-slide image level. Specifically, the dataset was randomly divided into training and validation sets 5 independent times, and the SCNN model was trained and evaluated separately for each split. Within each split, spectral images were cropped into non-overlapping patches of 40 × 40 pixels for network training, while ensuring that no patches derived from the same whole-slide image were distributed across different subsets. A total of 5 validation rounds were performed, and the final pathological classification results were obtained by averaging the outcomes from all rounds. The ROC curve was generated after each round of validation, and the AUC was computed to provide an overall measure of model performance.

The CNN model was implemented using PyTorch 2.6.0 and trained on an NVIDIA GeForce RTX 4060 GPU. The architecture consisted of four convolutional blocks designed for 9-channel hyperspectral inputs of size 40 × 40. Each block contained two 3 × 3 convolutional layers (with padding = 1) followed by batch normalization and ReLU activation, and a 2 × 2 max pooling operation for spatial downsampling. The numbers of feature maps in the four blocks were 32, 64, 128, and 256, respectively. After the final convolutional block, the feature maps (256 × 2 × 2) were flattened and fed into a fully connected layer with 128 units, followed by a ReLU activation and a dropout layer (dropout rate = 0.5). A final fully connected layer with 2 output neurons produced the logits for binary classification. Training was performed using a batch size of 64 and the Adam optimizer with an initial learning rate of 1×10^{-4} and a weight decay coefficient of 0.01 for L2 regularization. A StepLR learning rate scheduler was applied.

Abbreviations

DED	Dry eye disease
MGD	Meibomian gland dysfunction
SCNN	Spectral convolutional neural network
MGEX	Meibomian gland expressibility
TBUT	Tear film break-up time
CFS	Corneal fluorescein staining
OSDI	Ocular surface disease index
H&E	Hematoxylin and eosin
MG	Meibomian gland
Hb	Hemoglobin
NIR	Near-infrared
OCL	Optical convolutional layer
ENLs	Electronic neural layers
CMOS	Complementary metal oxide semiconductor
CIS	CMOS image sensor
OCUs	Optical convolutional units
t-SNE	T-distributed stochastic neighbor embedding
SEM	Scanning electron microscope
CNN	Convolutional neural network
ROC	Receiver operating characteristic
NMR	Nuclear magnetic resonance
AI	Artificial intelligence
AUC	Area under the spectral curve
PCA	Principal component analysis

Supplementary Information

The online version contains supplementary material available at https://doi.org/10.1186/s43074-026-00246-2.

Supplementary Material 1.

Acknowledgements
The authors thank Dr. Xiaowei Liu for his help in sample acquisition and Dr. Bo Chen for pathological section preparation.

Authors' contributions

Y. S. and T. L. contributed equally to this work. D.C. and K. C. conceived the study. Y. S. and T.L. conducted the experiments with the help of W. Y., Y.L. and Y. H. supervised the project. Y. D. and S. Y. assisted in collecting and preparing clinical samples, as well as collecting clinical information. Y. S. and T. L. wrote the manuscript with contributions from all other co-authors. All authors read and approved the manuscript.

Funding
This research was supported by National Natural Science Foundation of China (NSFC): grant number 82000863 (D. C.) and U22A6004 (Y. H.), and National Key Research and Development Program of China: grant number 2023YFB2806703 (Y. H.) and 2022YFF1501600 (K. C.).

Data availability

The data supporting the findings of this study are available from the corresponding author upon reasonable request.

Declarations

Competing interests

None declared.

Received: 25 September 2025 Revised: 3 March 2026 Accepted: 14 April 2026

References

1. Stapleton F, Velez FG, Lau C, Wolffsohn JS. Dry eye disease in the young: A narrative review. Ocul Surf. 2024;31:11–20.
2. McDonald M, Patel DA, Keith MS, Snedecor SJ. Economic and humanistic burden of dry eye disease in Europe, North America, and Asia: a systematic literature review. Ocul Surf. 2016;14:144–67.
3. Nelson JD, et al. The international workshop on meibomian gland dysfunction: report of the definition and classification subcommittee. Invest Ophthalmol Vis Sci. 2011;52:1930–7.
4. Tomlinson A, et al. The International Workshop on Meibomian Gland Dysfunction: Report of the Diagnosis Subcommittee. Invest Ophthalmol Vis Sci. 2011;52:2006–49.

5. Malonek D, Grinvald A. Interactions between electrical activity and cortical microcirculation revealed by imaging spectroscopy: implications for functional brain mapping. Science. 1996;272:551–4.
6. Desjardins M, et al. Preliminary investigation of multispectral retinal tissue oximetry mapping using a hyperspectral retinal camera. Exp Eye Res. 2016;146:330–40.
7. Kashani AH, et al. Noninvasive assessment of retinal vascular oxygen content among normal and diabetic human subjects: a study using hyperspectral computed tomographic imaging spectroscopy. Retina. 2014;34:1854–60.
8. Cui K, Huang Y. On-chip spectral imaging and sensing transition towards marketable technologies. Nat Rev Electr Eng. 2025;2:151–2.
9. Yang J, et al. Ultraspectral Imaging Based on Metasurfaces with Freeform Shaped Meta-Atoms. Laser Photonics Rev. 2022;16:2100663.
10. Xiong J, et al. Dynamic brain spectrum acquired by a real-time ultraspectral imaging chip with reconfigurable metasurfaces. Optica. 2022;9:461–8.
11. Cui K, et al. Spectral convolutional neural network chip for in-sensor edge computing of incoherent natural light. Nat Commun. 2025;16:81.
12. van Kampen EJ, Zijlstra WG. Spectrophotometry of hemoglobin and hemoglobin derivatives. Adv Clin Chem. 1983;23:199–257.
13. Pucker AD, Nichols JJ. Analysis of meibum and tear lipids. Ocul Surf. 2012;10:230–50.
14. Borchman D, et al. Physical changes in human meibum with age as measured by infrared spectroscopy. Ophthalmic Res. 2010;44:34–42.
15. Kim H, Cho KJ, Durkin AJ, Tromberg BJ, Park I. Quantitative measurement of optical properties and Hb concentration in a rodent model of inflammatory Meibomian gland dysfunction using spatial frequency domain imaging. Biomed Opt Express. 2022;13:1261–74.
16. Seen S, Tong L. Dry eye disease and oxidative stress. Acta Ophthalmol. 2018;96:e412–20.
17. Neugebauer U, März A, Henkel T, Schmitt M, Popp J. Spectroscopic detection and quantification of heme and heme degradation products. Anal Bioanal Chem. 2012;404:2819–29.
18. Horecker BL. The absorption spectra of hemoglobin and its derivatives in the visible and near infra-red regions. J Biol Chem. 1943;148:173–83.
19. Liu Y, et al. Hypoxia: a breath of fresh air for the meibomian gland. Ocul Surf. 2019;17:310–7.
20. Butovich IA, Millar TJ, Ham BM. Understanding and analyzing meibomian lipids–a review. Curr Eye Res. 2008;33:405–20.
21. Hwang HS, et al. Light transmission/absorption characteristics of the meibomian gland. Ocul Surf. 2018;16:448–53.
22. Borchman D, Foulks GN, Yappert MC, Tang D, Ho DV. Spectroscopic evaluation of human tear lipids. Chem Phys Lipids. 2007;147:87–102.
23. Borchman D, Foulks GN, Yappert MC, Milliner SE. Differences in human meibum lipid composition with meibomian gland dysfunction using NMR and principal component analysis. Invest Ophthalmol Vis Sci. 2012;53:337–47.
24. Wang J, Yeh TN, Chakraborty R, Yu SX, Lin MC. A deep learning approach for Meibomian gland atrophy evaluation in meibography images. Transl Vis Sci Technol. 2019;8:37.
25. Lin JW, et al. Meibomian glands segmentation in infrared images with limited annotation. Int J Ophthalmol. 2024;17:401–7.
26. Geerling G, et al. The international workshop on meibomian gland dysfunction: report of the subcommittee on management and treatment of meibomian gland dysfunction. Invest Ophthalmol Vis Sci. 2011;52:2050–64.
27. Wolffsohn JS, et al. TFOS DEWS III: diagnostic methodology. Am J Ophthalmol. 2025;279:387–450.
28. Vidas Pauk S. Noninvasive tear film break-up time assessment using handheld lipid layer examination instrument. Acta Clin Croat. 2019;58:63–71.
29. Tsubota K. Short Tear Film Breakup Time-Type Dry Eye. Invest Ophthalmol Vis Sci. 2018;59:Des64-des70.
30. Hykin PG, Bron AJ. Age-related morphological changes in lid margin and meibomian gland anatomy. Cornea. 1992;11:334–42.
31. Duarte TF, Siqueira RC. Clinical-epidemiological profi le, risk factors and quality of life of patients with meibomian gland dysfunction. Rev bras.oftalmol. 2025;84:e0033.
32. Bron AJ, Evans VE, Smith JA. Grading of corneal and conjunctival staining in the context of other dry eye tests. Cornea. 2003;22:640–50.
33. Miller KL, et al. Minimal clinically important difference for the ocular surface disease index. Arch Ophthalmol. 2010;128:94–101.
34. Tunon-Robinson I, Huang J, Xu X, Nguyen AK. Visual performance of individuals with and without meibomian gland dysfunction. Cureus. 2025;17:e81655.

Publisher's Note